Supplementary Materials

1. Discussion: Open questions and unresolved issues

The epithelial layers studied here are diverse, complex, and biologically relevant, but they are not to be confused with cell collectives that fully pack three-dimensional space. In that connection, the extracellular matrix (ECM) would be expected to provide local adhesive footholds for development of cell traction forces. But at the same time, ECM fibers would impose steric impediments to cell migration, screen force transmission from cell-to-cell, and induce cell channeling, all of which would be expected to impact cell jamming dynamics.[38,49,50] Although cells might migrate on a basement membrane, the native tissues of central interest in this report –the human bronchial epithelial layer and the *Drosophila* embryonic epithelial layer– are otherwise constitutively devoid of ECM, as are many epithelial tissue compartments. Importantly, epithelia tend to be disordered and isotropic within in the cell layer plane, whereas, for example, the vascular endothelium subjected to shear flow becomes highly ordered and anisotropic[51], in which case geometric relationships as reported here would likely take a form that is quite different. In epithelia, unjamming and associated changes in cell geometries may represent a physical requirement for cell migration and cell rearrangements; to rearrange among themselves the cells within the layer must change shape and the distribution of these shapes. But the relationship of unjamming to migratory events, the energetic efficiency of cell migration, and cell metabolism remain unclear. In HBECs, for example, proximity to the jammed state and the character of swirling motions have been shown to be tightly connected, and the tendency toward unjamming in asthma is suggestive of an injured or dysmature epithelial phenotype.[4] In cases such as the *cta* mutant and *twist* knockdown in the *Drosophila* embryo (Fig. 2), by contrast, cell geometries are clearly indicative of unjamming but collective migration is attenuated or unapparent, seemingly because formation of the ventral furrow has been impeded and associated tugging forces near the fold have diminished. In that connection, neighbor-swapping in a fully jammed collective is impossible, but the solid-like cellular collective might nevertheless be able to migrate *en bloc*, much as in the rotation of the *Drosophila* egg chamber driven by follicular epithelial cells.[52] Importantly, in the contexts of development, cancer, and the metastatic cascade, cells are thought to attain motility often through the agency of an epithelial-to-mesenchymal transition (EMT),[53,54] but it remains unclear if unjamming might or might not fit within the EMT continuum.[53,55,56] The manner in which progenitor cell content, cell proliferation, cell extrusion from the layer, contact inhibition, and apoptosis might impact –and be impacted by– jamming dynamics are unknown.[34,57-60] Finally, it has yet to be established if the systematic geometrical features reported here might find practical application in examination of tissue specimens in clinical pathology.

2. *Supplementary Data*

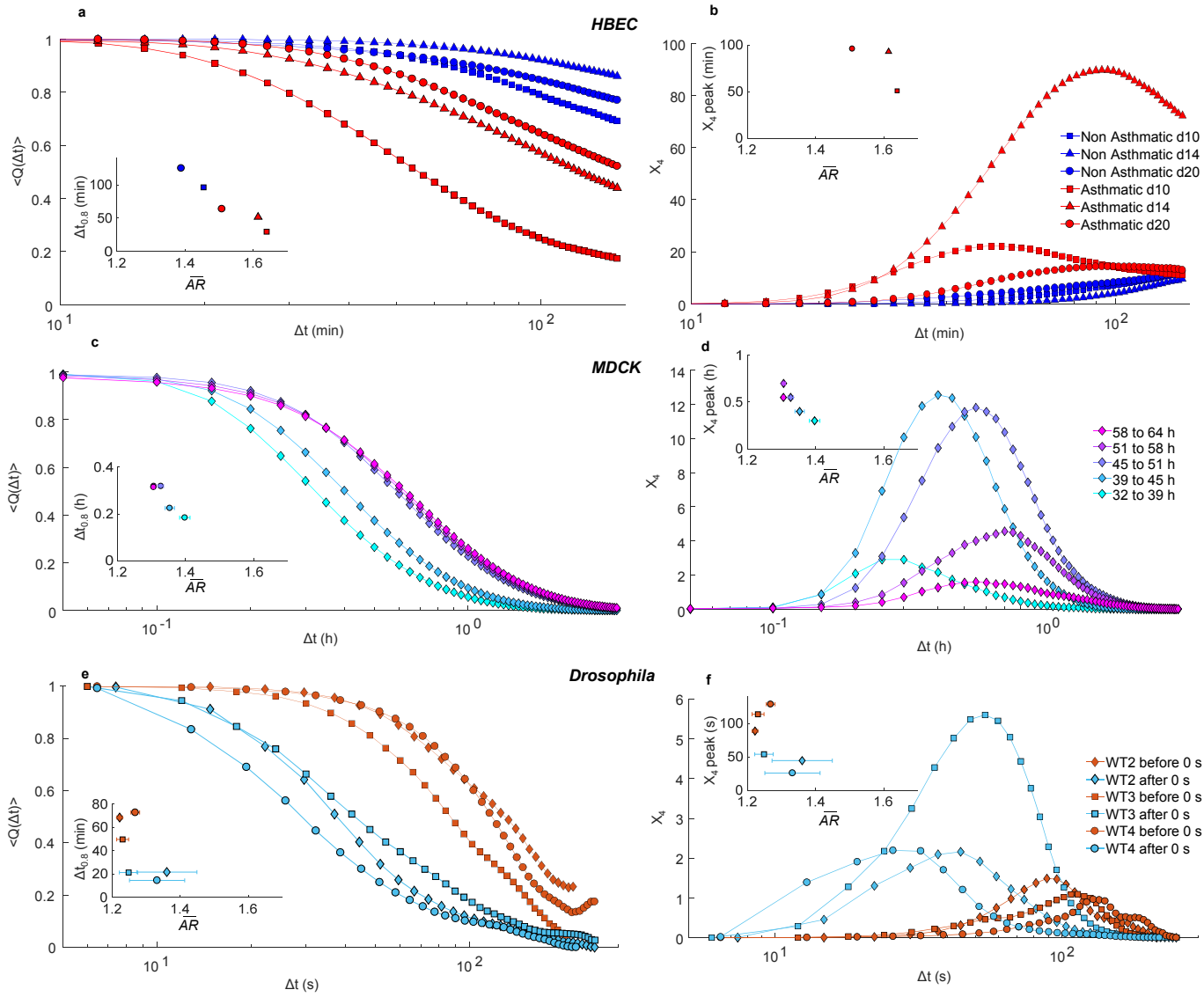

Figure S1| Migratory Dynamics for HBEC, MDCK and *Drosophila.*
To quantify migratory dynamics in datasets for HBECs, MDCKs, and *Drosophila*, we computed the self-overlap order parameter $Q(\Delta t)$ and the four-point susceptibility $X_4(\Delta t)$ as described previously.[4]
Collective dynamics of HBECs: **a**, Consistent with previous characterizations[4], non-asthmatic cells retain a larger self-overlap, indicate of less motion, over longer timescales than do asthmatic cells. Inset: There is an inverse trend between the timescale at which the self-overlap order parameter crosses 0.8 (referred to as $\Delta t_{0.8}$).
b,The peak of the four-point susceptibility $X_4(\Delta t)$ corresponds to the timescale and size of a collective pack.[61] Here again our results are consistent with previous characterizations, with non-asthmatic cells not exhibiting any observable peak or lifetime within the experimental window, indicating low motility. Inset: There is an inverse trend between X_4 peak time and $\overline{AR}$.
Collective dynamics of MDCKs: c, Data is separated intervals of 6-7 hours as the cells approached confluence. Similar to HBECs, cells retain higher self-overlap as the system approaches confluence. Inset: There is a roughly inverse trend between $\Delta t_{0.8}$ and $\overline{AR}$. **d**, MDCK cells show higher pack lifetimes as the system approaches confluence, as can be estimated from the peak of the $X_4(\Delta t)$ values. Inset: There is a roughly inverse trend between X_4 peak time and $\overline{AR}$.
Collective dynamics in WT *Drosophila* embryos: Compared with events occurring in HBECs and MDCKs (hours-days), events typifying ventral furrow formation in the *Drosophila* embryo are much faster (second-minutes). Due to formation of the furrow and ancillary events, moreover, the system cannot be considered to be even approximately statistically stationary or quasi-static. In a few WT embryos, however, images were collected before

myosin levels rose and the furrow started to form, an interval which could be considered approximately quasi-static (labelled before 0 seconds); these are compared with corresponding datasets as the furrow starts forming (labelled after 0 seconds). **e**, Before the furrow starts forming as compared to during, cells retain higher overlap for longer timescales. Inset: There is a roughly inverse trend between $\Delta t_{0.8}$ and $\overline{AR}$. **f**, Similarly, before the furrow starts forming as compared to during, cells show higher pack lifetimes, as can be estimated from the peak of the $X_4(\Delta t)$ values. Inset: There is a roughly inverse trend between X_4 peak time and $\overline{AR}$.

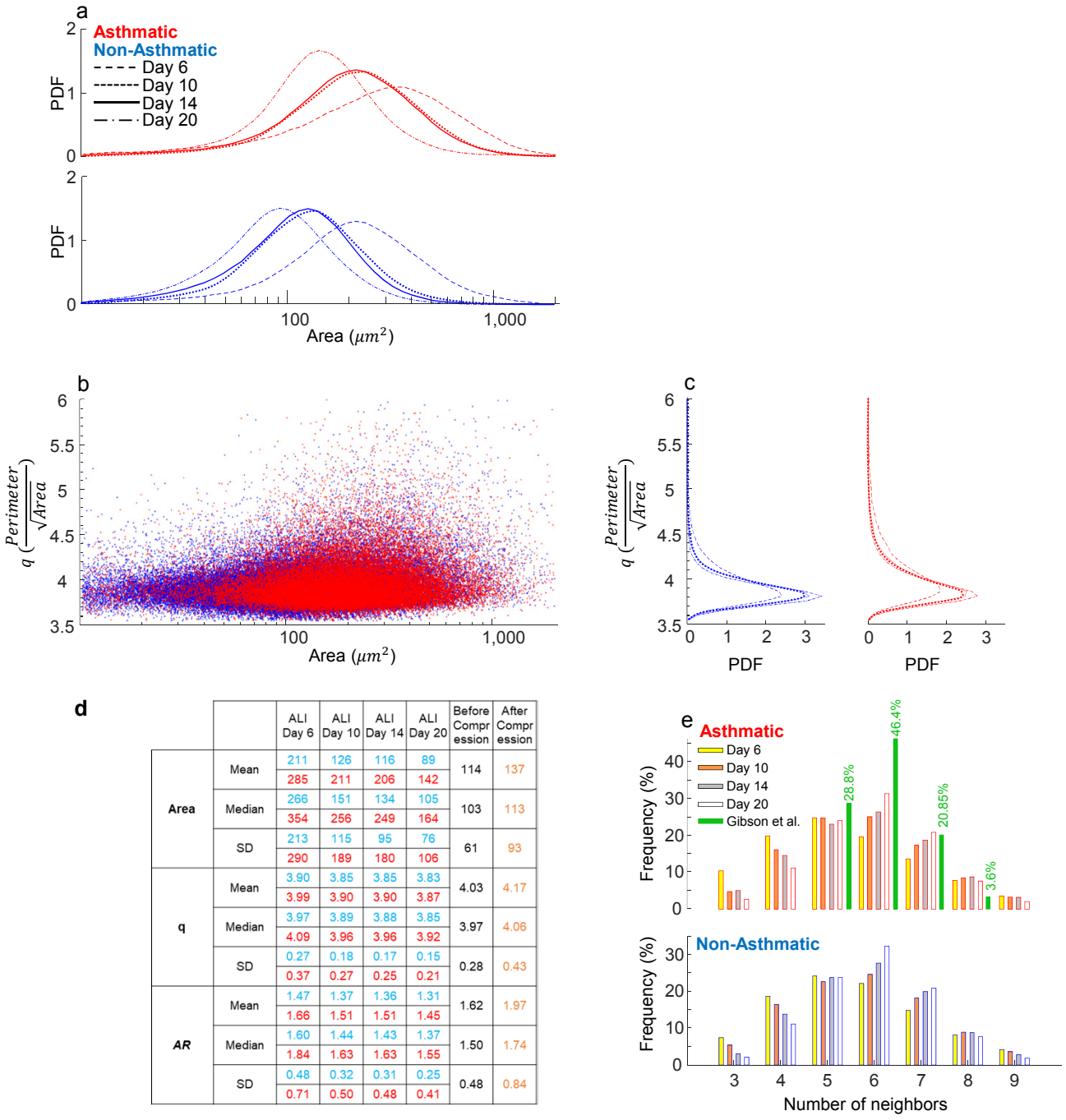

		ALI Day 6	ALI Day 10	ALI Day 14	ALI Day 20	Before Compression	After Compression
Area	Mean	211	126	116	89	114	137
		285	211	206	142		
	Median	266	151	134	105	103	113
		354	256	249	164		
	SD	213	115	95	76	61	93
		290	189	180	106		
q	Mean	3.90	3.85	3.85	3.83	4.03	4.17
		3.99	3.90	3.90	3.87		
	Median	3.97	3.89	3.88	3.85	3.97	4.06
		4.09	3.96	3.96	3.92		
	SD	0.27	0.18	0.17	0.15	0.28	0.43
		0.37	0.27	0.25	0.21		
AR	Mean	1.47	1.37	1.36	1.31	1.62	1.97
		1.66	1.51	1.51	1.45		
	Median	1.60	1.44	1.43	1.37	1.50	1.74
		1.84	1.63	1.63	1.55		
	SD	0.48	0.32	0.31	0.25	0.48	0.84
		0.71	0.50	0.48	0.41		

Figure S2| Distributions of cell size and shape metrics differ between asthmatic and non-asthmatic HBECs. **a**, Across non-asthmatic and asthmatic HBECs, and across all days of maturation, cell area was broadly distributed. As cell numbers proliferate with layer maturation these distributions shift to the left (Fig. 1a, 1st and 3rd rows). For each ALI day, cell area of asthmatic HBECs was greater than for non-asthmatics. **b**, In both asthmatic (n=46,076 cells) and non-asthmatic (n=87,066 cells) HBECs, the shape metric q (perimeter/$\sqrt{\text{area}}$) was highly variable but did not co-vary with projected cell area (cf. Fig.1b). **c**, PDFs of *q* became systematically less skewed and less variable with maturation. For every given ALI day, *q* of the asthmatic HBECs was higher than for the non-asthmatic ones. **d**, Median, Mean, and standard deviation (SD) of both cell area and cell shape metrics, *q* and *AR*, became progressively smaller with increasing days of maturation and their respective distributions became less variable (**a**, **c**, Fig. 3a). Consistent with previous report, at day 20 of ALI the non-asthmatic cells attained a median *q* value of 3.83, similar to the critical *q* value associated with jammed epithelial layers.[4] Upon compression, consistent with Figure 1, the median, mean, and standard deviation of cell shape metrics increase dramatically, and cell areas increase slightly. **e**, Most cells had 5 or 6 immediate neighbors, although the number of nearest neighbor

was often as small as 3 or as large as 9. With layer maturation the distribution of nearest neighbors became somewhat more tightly clustered around 6, but did not differ between non-asthmatic and asthmatic HBECs. These distributions were substantially wider than the predicted nearest-neighbor equilibrium distribution in proliferating epithelia from Gibson et al.,[11] shown in green.

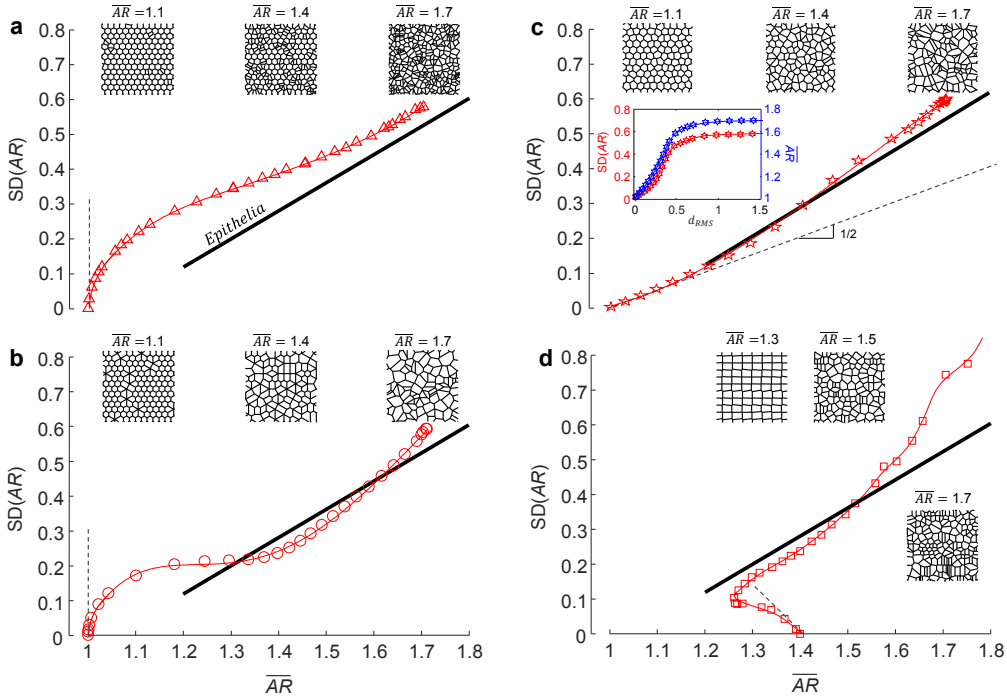

Figure S3| Mathematics of random tiling roughly describes certain facets of the observed geometrical relationship but fails to explain it.

To explain our findings at the simplest possible level, we resorted solely to the mathematics of tessellation and imposed randomness. We did so by constructing a variety of mathematical families of random tessellations in the plane. In each panel above, the empirical relationship described in the main text is represented as a solid black regression line based upon data in Figs. 1-2. As described below, we have constructed mathematical families of random tessellations in the plane. For each such mathematical construct we computed the relationship between SD(*AR*) and $\overline{AR}$ with graded degrees of imposed structural randomness. In each panel above, the broken line depicts the slope predicted in the limit that imposed structural randomness is vanishingly small.

Each mathematical construct can be argued to recapitulate roughly certain facets of the empirical observations. As such, these mathematical constructs might provide a partial explanation. Nevertheless, it is important to recognize that these constructs provide no physical mechanism, and may even confuse cause with effect. Crucially, for example, they offer no mechanism to explain the level of randomness, and thus set the position of a given system along the relationship. More importantly, among all packing geometries in the plane that are mathematically allowable, these constructs provide no mechanism to explain which geometries might be physically allowable. Dynamically, these mathematical constructs by themselves offer no mechanistic connection between cellular migration and packing geometries, or between packing geometries and the transmission of physical forces.

As shown in Fig. S4, and discussed in the main text, the jamming mechanism imposes physical constraints that address all these issues. More importantly, if jamming and jammed packings are the cause of the randomness, then imposed structural randomness in these mathematical constructs might describe observations. But being the effect and not the cause, this imposed randomness would fail to explain those observations mechanistically.

Random departures from regular hexagonal tiling:

a, Random addition of seed points: Starting from a regular hexagonal tiling, we took the center of each hexagon as a seed point. We then randomly added seed points, which created defects in an otherwise regular seeding lattice, and then used Voronoi tessellation to generate a new tiling (△). Representative tilings are shown in insets. As progressively more random seed points are added, the relationship between SD(AR) and AR follows is non-linear (red line) and differs from that observed in epithelial layers (black line). In the limit that the number of added random points is very large, $\overline{AR}$ approaches 1.7, which corresponds to random Poisson seeding.

b, Random deletion of seed points: Starting again from a regular hexagonal pattern, we randomly deleted seed points, again creating defects in an otherwise regular seeding lattice, and then used Voronoi tessellation to generate a new tiling (○). Representative tilings are shown in insets. As progressively more random seed points are deleted, the relationship between SD(AR) and AR is non-linear curve (red line) and differs from that observed in epithelial layers (black line). In the limit that the number of deleted random points is very large, $\overline{AR}$ again approaches 1.7, corresponding again to random Poisson seeding.

c, Random displacement of seed points: Starting from a regular hexagonal pattern, we kept the number of seed points fixed but imposed upon each seed point a random displacement. These random displacements (relative to hexagonal side length) were characterized by their root mean square value, d_{RMS}. d_{RMS} was progressively increased and we then used Voronoi tessellation to generate a new tiling (☆). Representative tilings are shown in insets. As d_{RMS} increases the relationship between SD(AR) and AR follows a non-linear curve (red line) that approximates that observed in epithelial layers (black line). When $d_{RMS} \ll 1$, SD(AR) and AR increase in tandem (insets). In this limit hexagons become increasingly distorted but the tessellated network exhibits no change in topology. Moreover, in this limit the distribution of ARs is not skewed and is poorly fit by a k-gamma distribution (not shown). As d_{RMS} approaches order of unity, however, both SD(AR) and AR increase more slowly with increasing d_{RMS}, and the tessellated network increasingly displays alterations in network in topology. In the limit that $d_{RMS} \gg 1$, both SD(AR) and AR saturate at values corresponding to random Poisson seeding. In that limit the distribution of ARs becomes highly skewed and well-fit by a k-gamma distribution (not shown).

Random departures from a regular rectangular tiling:

d, Seed points were arranged in equally spaced horizontal rows. Along each row, the distance between seeds, w, was distributed in a log-normal fashion $\left(w \sim LN(\mu = 0.33,\ 0 \le \sigma \le 0.5)\right)$. We then used Voronoi tessellation to generate a new tiling(□). σ = 0 corresponds to a regular rectangular grid. In that case $\overline{AR}$ =1.4= e^{μ} and SD(AR) =0. As σ increased by a small amount from 0, SD(AR) increased but $\overline{AR}$ decreased (dash-dot line). Note the negative initial slope. As σ further increased, however, relationship between $\overline{AR}$ and SD(*AR*) was neither linear nor monotonic

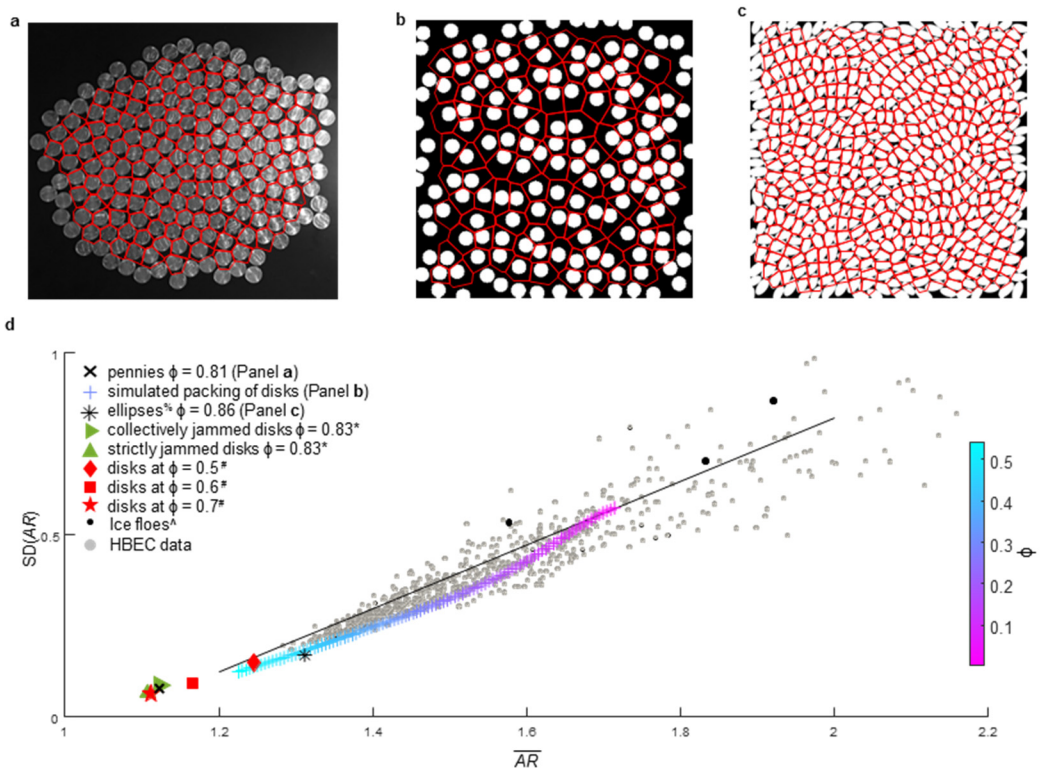

Figure S4| Jamming in inert granular 2D systems conform to the same packing geometries as do HBECs. In Fig. S3 we show that imposed structural randomness in mathematical constructs might describe certain facets of the observed geometrical relationship. But if jamming and jammed packings are the cause of the randomness, then such imposed randomness would confuse cause with effect, and thus fail to explain those observations mechanistically.

Starting from a jammed hexagonal lattice, as in the case of close-packed rigid circular discs, each jammed disc is constrained to zero translation degrees of freedom, and therefore can accommodate no displacement relative to its neighbors; in a fully jammed regular system, such postulated random displacements are not allowable. In such a system, therefore, jamming imposes upon the randomness a strong a geometric constraint.

Using Voronoi tessellation based upon centers of constituent particles in a variety of systems at different packing fractions (ϕ), we created a complete polygonal tiling of the occupied surface to generate equivalent cells. Cell aspect ratio (*AR*) was measured (Fig. S10) to obtain a relationship between the variability of cell *AR* and its mean in these non-confluent systems.

a, Discs (pennies) randomly packed on a surface (ϕ = 0.81). **b,** Random sequential addition of disks;[62] ϕ approaching zero corresponds to random tiling of Poisson seeds. **c,** Randomly packed ellipses (ϕ = 0.86)[% 63]. **d,** *AR* from all systems defined a clear relationship between the standard deviation (SD) of *AR* and its mean, independent of ϕ. Each gray datum represents a different field of view for both asthmatic and non-asthmatic HBEC. In addition, other systems of disks with higher packing fraction * [64,65] and ice floes from the Arctic region follow the same relationship.[^ 66] (Symbols %, *, ^,# correspond to references indicated.)

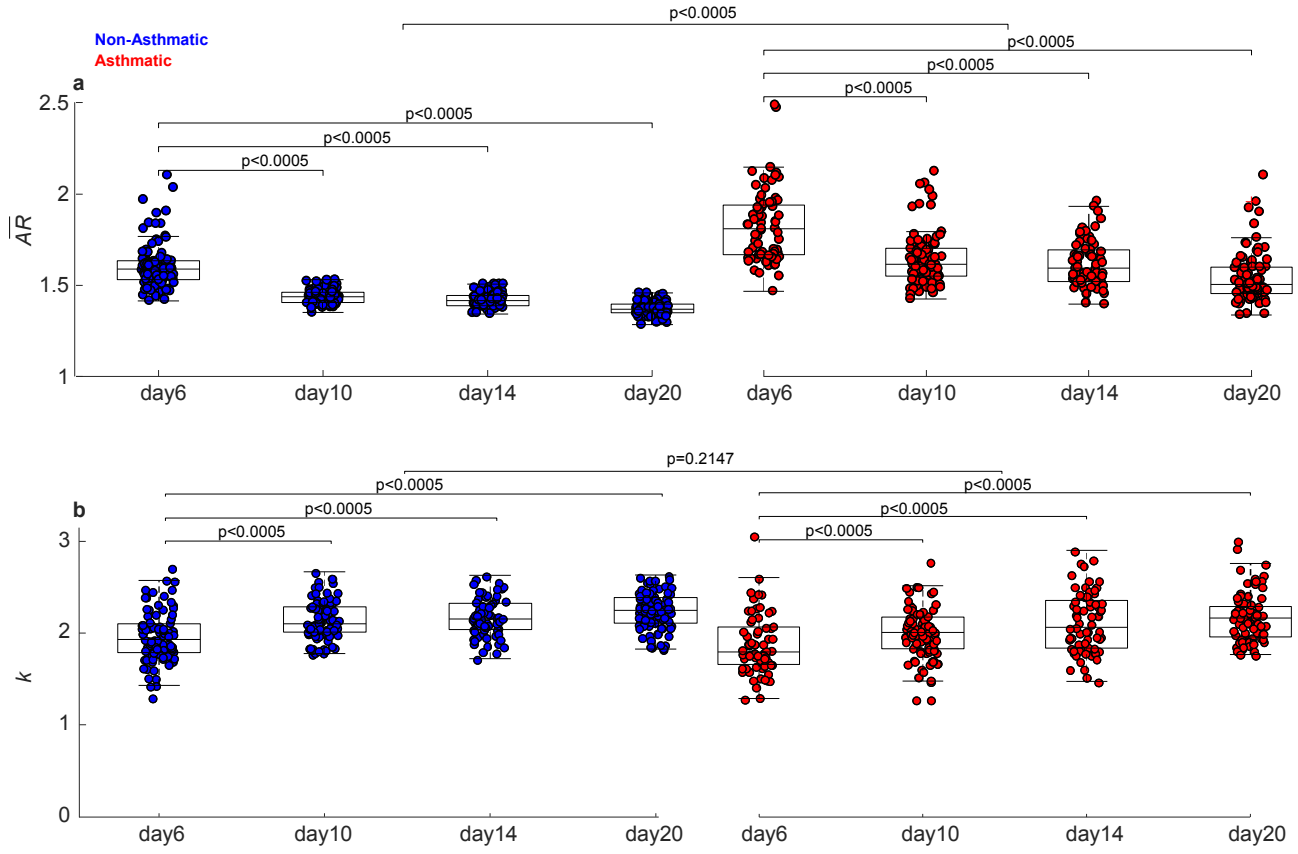

Figure S5| $\overline{AR}$ and *k* characterize cell shape distributions of HBECs.

a, For both non-asthmatic and asthmatic HBECs, $\overline{AR}$ became progressively smaller with increasing days of maturation (p<0.0005), and across all days $\overline{AR}$ of the asthmatic HBECs was larger than for non-asthmatic ones (p<0.0005). (Each datum represents a different field of view). **b**, PDFs of the rescaled AR (Fig. 3) followed the *k*-gamma distribution (Eq.1), analytically described by a single parameter, *k*. A common value of *k*=1.97 was observed across all days of maturation and across non-asthmatic and asthmatic HBECs (p=0.2147). (Each datum represents a fitted *k* value determined by maximum likelihood estimation, MLE, for each individual field of view).

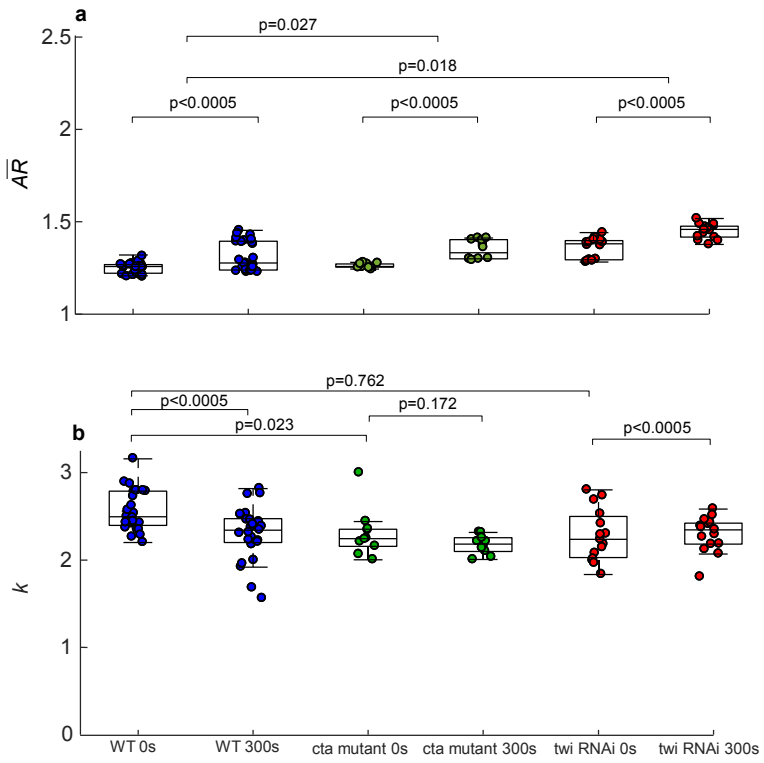

Figure S6| $\overline{AR}$ and *k* characterize cell shape distributions during ventral furrow formation in *Drosophila in vivo.*

a, For wild type (WT), cta mutant and twist (twi) RNAi embryos (n = 5, 2 and 3 respectively), $\overline{AR}$ increased with time (p<0.0005). Each datum represents a single frame from a sequence of five consecutive frames (~40s) in the vicinity of the specified time point (x-axis ticks). b, PDFs of all rescaled AR data (Fig. 3) followed a k-gamma distribution (Eq.1), analytically described by a single parameter, k. (Each datum represents a fitted k value for a single frame). *k* slightly decreased with time in the cases of Wild Type and *twist* knockdown embryos (p<0.0005), yet a common value of *k*=2.52 (p=0.023) was observed across all.

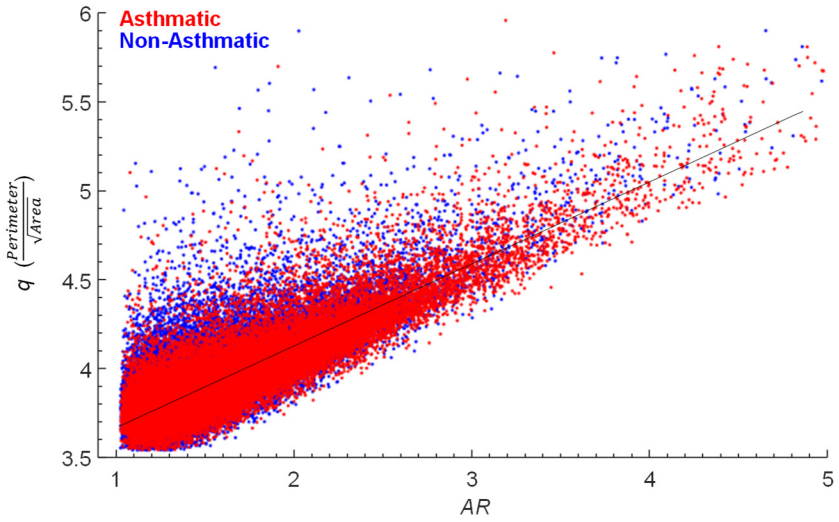

Figure S7| Two different shape factors -*AR* and *q*- are correlated, but *AR* expresses a larger experimental range.

For any closed ring in the cell plane, the aspect ratio *AR* serves as a simple, primitive, and robust metric of shape (see Fig. S10). In a previous study we had used as an index for shape the factor, *q*, which is the ring perimeter divided by the square root of area.[4] In the dataset in this report *AR* and *q* are correlated; in both asthmatic (n=46,076, red symbols) and non-asthmatic (n=87,066, blue symbols) HBECs, the shape factor *q* (cell perimeter/ $\sqrt{\text{area}}$) and the shape factor *AR* were roughly correlated ($q = 0.433AR+3.25$; $R^2=0.687$). Because *AR* is based moments of cell areas (Fig. S10) rather than cell perimeter, it is less sensitive than is *q* to errors in identification of cell boundary pixels. More importantly, the experimentally observed range of *AR* was found to span roughly five-fold (from 1 to 5) whereas that of *q* spanned less two-fold (from 3.5 to 6). To better resolve small changes in cell shape, in this report we use *AR*.

	Slope of SD(AR) vs AR			
	Slope	95% lb*	95% ub*	p-value
Non Asthmatic HBEC				
Day 6	0.888	0.813	0.964	<0.0005
Day 10	0.913	0.788	1.038	<0.0005
Day 14	0.921	0.784	1.058	<0.0005
Day 20	0.799	0.666	0.931	<0.0005
Asthmatic HBEC				
Day 6	0.717	0.660	0.773	<0.0005
Day 10	0.715	0.645	0.786	<0.0005
Day 14	0.710	0.621	0.799	<0.0005
Day 20	0.592	0.517	0.668	<0.0005
MDCK				
All time	0.870	0.860	0.880	<0.0005
Drosophila				
Wild Type 0s	0.9276	0.8726	0.9825	<0.0005
cta mutant 0s	0.9977	0.8264	1.1690	<0.0005
twist RNAi 0s	1.3147	1.1752	1.4542	<0.0005
***Drosophila:* Change in slope per 100 seconds**				
Wild type	0.9280	0.9104	0.9448	0.960
cta mutant	1.0028	0.9807	1.0147	0.553
twist RNAi	1.3203	1.3000	1.3294	0.461

Table S1| **Slope of standard deviation of *AR* vs its mean**. In the first four groups of rows, p-value is the probability that the slope is zero; in the fifth group, p-value is the probability of the indicated change in the slope over every 100 seconds of the observation window. Slope: the slope of SD(*AR*) vs $\overline{AR}$; lb*: lower confidence bound; ub*: upper confidence bound.

3. *Air Liquid Interface Culture*

The human conducting airways are lined by a pseudostratified layer of epithelial cells comprised of multiple cell types, including basal, goblet, and ciliated cells. These cell types are defined by location, function, and expression of cell type specific markers.[67] The pseudostratified epithelium sits on and contacts with a basement membrane composed of collagens and lamins. Basal cells are progenitor cells of the airway epithelial cells and are identified by the positive staining of NGFR protein and by the expression of transcription factor, TP63. Goblet cells and ciliated cells form the functional apparatus collectively referred to as the mucociliary escalator, in which pathogens are trapped in mucus secreted by goblet cells and cleared by the coordinated beating of cilia in the airways. Goblet cells are identified by the presence of mucin-containing granules positively stained for MUC5AC protein and by the expression of transcription factor, FoxA2. Ciliated cells are identified by the presence of cilia positively stained for β-tubulin IV protein and the expression of transcription factor, FoxJ1. Culture in air-liquid interface of primary basal cells from human donors recapitulates the pseudostratified structure of the intact human airway epithelium, and is considered the gold standard in studying airway epithelial biology.[68]

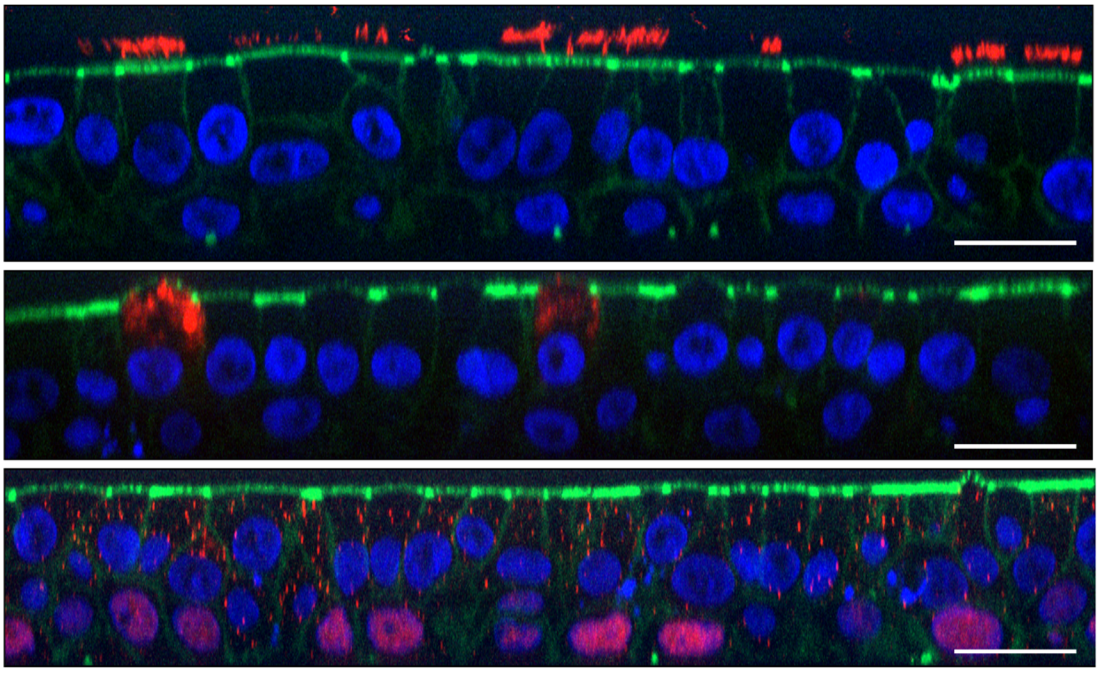

Figure S8| Human bronchial epithelial cells form a pseudo-stratified layer. Side-view images were reconstructed from z-stacks taken of HBEC layers fixed and stained on ALI day 20. In all three panels, green stains for F-actin, and blue stains for cell nuclei. In the top panel, the red color stains for β-tubulin IV which is a marker of ciliated cells. In the middle panel, red stains for MUC5AC which is a marker for goblet cells. In the bottom panel, red stains for p63 which is a marker of basal cells, and in some cases found in the nuclei and thus leads to a pink color. Scale bars are 20 μm. The multiple z-positions of nuclei and cell features in these different kinds of are the typical appearance of a pseudostratified layer.[69]

4. Algorithm for identification of cell boundaries:

To determine cell boundaries we used a semi-automatic segmentation pipeline. Intermediate results are depicted in Fig. S9. These included: **(a)** correction for non-uniform illumination by subtracting from the image its background, identified using *imopen* function in Matlab; boundaries were then enhanced according to the ratio between eigenvalues of local Hessian matrices;[70] **(b)** application of an intensity threshold limit of about 95% followed by a manual correction for disconnected boundaries; boundaries were then thinned, and spur pixels (resulting from irregularities in the original boundary) and isolated pixels were removed using *bwmorph* function in Matlab; the skeletonized image was then blurred using a Gaussian filter followed by a 99% intensity threshold; *bwboundaries* function in Matlab was then used to produce the final segmented image. **(c)** We defined a cell object boundary by the set of interior pixels which shares an edge with at least one exterior pixel, as also illustrated in Fig. S10.

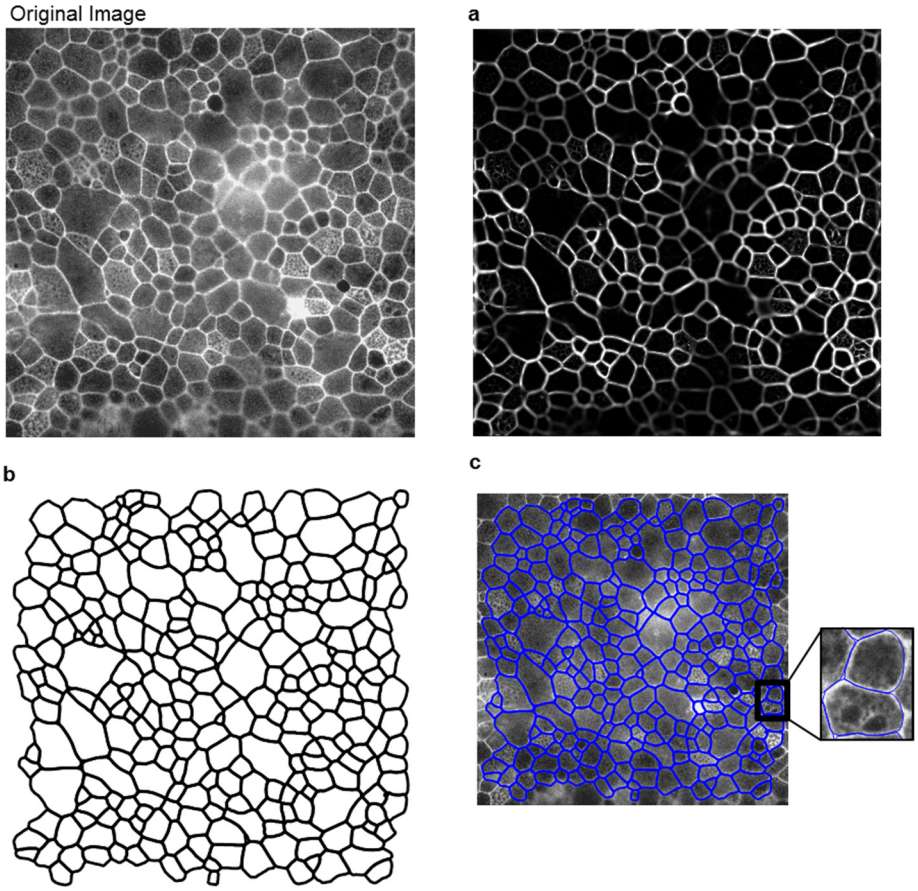

Figure S9| Identification of cells boundaries from an Epifluorescence image. **a**, Cell boundaries enhancement. **b**, Segmented image. **c**, Cell boundaries overlaid on the original image.

Algorithm for shape measurement*:* To measure cell areas and perimeters we adapted an approach taken by available commercial software.[71] For each identified cell i in the final segmented image, the algorithm constructed a polygon whose vertices lie along cell boundary pixels (Fig. S10a). The polygon's j^{th} side length is $1 \leq L_j \leq R_i$, with $R_i \equiv \max\left(0.1\sqrt{N_i}\,, 1.42\right)$, and N_i is the total number of pixels composing the cell object. We defined the area and perimeter of cell i as those of the polygon. The same polygon was used to evaluate the aspect ratio (*AR*) of cell i as $\frac{a}{b} \geq 1$ (Fig. S10b), which is the ratio between the major and the minor axes of an equivalent ellipse, with equal eigenvalues of the second area moments as those of the polygon.

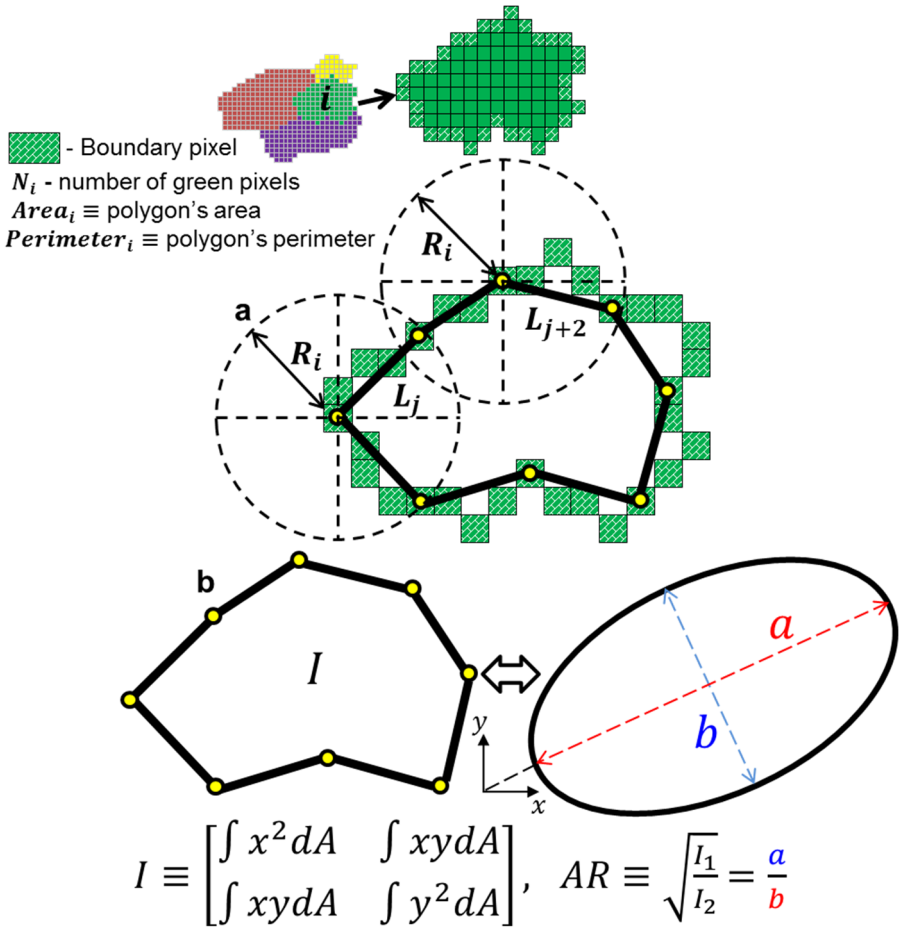

Figure S10| Shape and area measurements of cell *i*. Note that this is for illustration only, and a typical cell object is composed from thousands of pixels. **a**, Measurements of area$_i$ and perimeter$_i$ from a representative polygon with its vertices located along identified boundary pixels. **b**, An equivalent ellipse with equal eigenvalues (I_1 and I_2) of the second area moment I as of the polygons. The cell's aspect ratio (*AR*) is defined as $\frac{a}{b}$. Comparing this with *AR* measured using all boundary pixels, shows no systematic difference with cell area nor shape, with RMS of differences ~0.9%.

***Validation of algorithm performance**:* We measured *AR* and *q* (perimeter/$\sqrt{\text{area}}$), both manually using imageJ software (National Institutes of Health) and automatically using the algorithm for shape measurement. Cell boundaries in blurry regions (Fig. S11b,c) were not properly identified. We attribute this to local height variabilities in the layer causing these regions to be out of focus. The accuracy of the algorithm was evaluated by comparing the histograms between the automatic and the manual measurements which showed closely similar shapes and an order of 1% difference in mean, median and standard deviation of both *AR* and *q* (Fig. S11d,e).

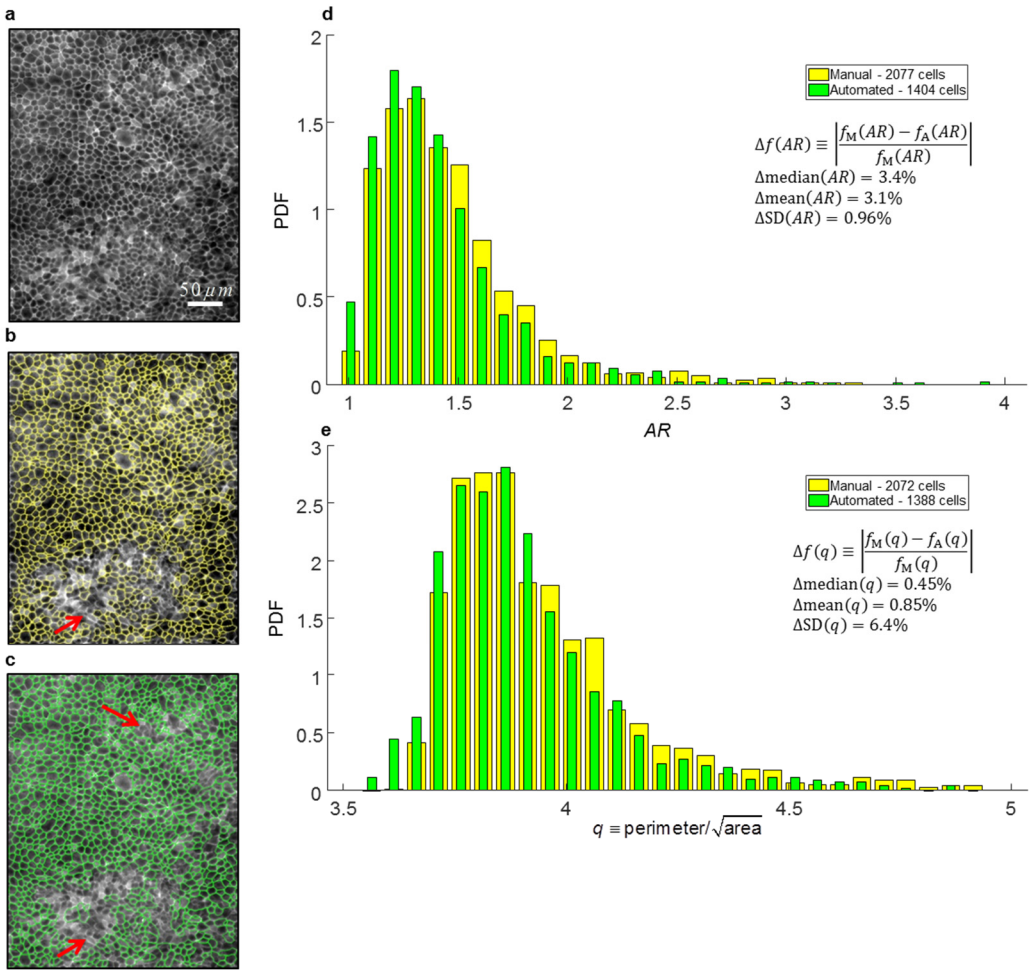

Figure S11| Automatic vs. manual detection of boundaries.
a, A typical Epifluorescence image of fixed primary HBECs labeled for cortical actin. **b**, Manual tracing of boundaries in ImageJ overlaid on the original image. **c**, Automatic detection of boundaries using our segmentation pipeline overlaid on the original image. Red arrows in b&c point to regions in which cells boundaries were not properly traced. **d**, **e**, Comparing automatic vs. manual shape measurements. The histograms for *AR* (with bin size of 0.1) and for *q* (with bin size of 0.05) considers cell objects which were filtered such that $10\mu m^2 \leq$ Cell Area $\leq 2000\mu m^2$, $AR \leq 4$ and $q \leq 5$. Typically most objects filtered out are small circular blobs, or multiple cells identified as one clump. The upper inset shows the resulted number of cells after filtration in each set. These are not identical since *q* and *AR* only roughly correlate (Fig. S7). The lower inset shows the relative difference Δf between different statistical moments $f_{M\backslash A}$ of the Automatic and the Manual measurements sets.

5. Ruling out artifacts

We considered that the consistency of the relationship decribed in the main text might reflect, 1) a peculiarity of HBECs, 2) an idiosyncrasy of layer maturation, or 3) simply an artifact of cell culture. To address the first possibility, we examined another cell type, the Madin-Darby canine kidney (MDCK) cell. Using Voronoi tessellation based upon nuclear centers, which approximates the position of cell-cell junctions in that system[72], we created a polygonal tiling of the cell layer from which we quantified cell *AR*. We complemented this tessellation analysis with manual tracing of cell boundaries from phase-contrast images, and quantified *AR* from these boundaries. In the case of maturing MDCK cells, much as in the case of maturing HBECs, with progressive cell jamming cellular speeds progressively decreased and shape analysis traced the same linear relationship of decreasing $\overline{AR}$ and SD(*AR*) (Video S1), thereby ruling out the first possibility.

To rule out idiosyncrasies of layer maturation, we studied changes in cell shape and shape variability that occur acutely in response to an imposed mechanical perturbation. Mature HBECs are known to be mechanosensitive in a manner that contributes to pathological remodeling of the asthmatic airway.[37,73] Therefore, to perturb the mature jammed HBEC layer we applied an apical-to-basal pressure difference ($30 cm H_2O$) across the porous transwell. This pressure difference mimics the mechanical compression that occurs *in vivo* during acute asthmatic bronchospasm.[36,37] Such compression shrinks the lateral intercellular space between adjacent epithelial cells, and, through pathways that have yet to be established, ultimately leads to elongated cell shape, unjamming of the layer, and increasing cell migration.[4,37,73] Whereas maturation caused changes in cell shape that tracked in time from larger $\overline{AR}$ and SD(*AR*) to smaller, indicative of progressive jamming, mechanical compression caused changes in cell shape that tracked in the opposite direction with time, from smaller $\overline{AR}$ and SD(*AR*) to larger, indicative of unjamming (Fig. 1f). Comparing unjamming *vs.* jamming these changes with time were opposite in sign, but tracked up or down a geometric relationship that in both instances was the same (cf. Fig. 1e and 1d).

To complement results from HBEC compression, we applied sequential stretches to the mature MDCK layer plated on a deformable substrate (6% strain amplitude, isotropic in the cell plane, 1s duration, once every 6s for 20 min). Immediately after stretch cessation, cell shapes became elongated, but within 60 min these changes relaxed back to pre-stretch values (Fig. 1f). Accordingly, in the cases of both HBEC compression and MDCK stretch, the $\overline{AR}$ and SD(*AR*) increased in concert to trace the same geometric relationship as observed during layer maturation, but exhibited an opposite trend to layer maturation with time (Fig. 1d,e,f). Moreover, these acute changes could not be accounted for solely by changes in cell crowding, which were small (Fig. S2d for HBECs). As such, the geometrical relationship traced by the data of Fig. 1d,e,f is not limited to HBECs, and is not a specific effect of the passage of time, layer maturation, or cell crowding; these factors all mattered but no one among them account for the observed geometric relationship.

6. Theoretical Predictions

Detailed computational models incorporating specific descriptions of cell elastic deformation, tension, adhesion, and propulsion are found to conform to this generic physical picture. For example, the cell jamming models of Bi *et al.* propose that there exists a preferred cell shape that is set by interactions among those factors (Fig. S12).[9,25,26,74,75] We note, however, that in the limit that cortical tension is very small the cell wall contours in real cells can fluctuate appreciably and diverge substantially from the polygonal shapes assumed in these and related computational models; in our data analysis, however, we did not assume polygonal cell shapes, and we did not observe such behavior. According to these computational models, and supporting observations,[76] contraction versus adhesion are then in competition because the former acts to reduce the length of each cell-cell junction whereas the latter acts to increase it. When cortical tension dominates, the collective is predicted to become solid-like and jammed. As a result, each cell becomes trapped in a shape that departs from its preferred shape, and $\overline{AR}$ becomes frozen at a value close to 1.2 (Fig. S12). As cell-cell adhesive effects progressively increase (or, equivalently, as cortical contractile effects progressively decrease), cell shapes remain trapped until some critical condition is ultimately reached. At that critical point the collective undergoes a transition from a solid-like jammed phase to a fluid-like unjammed phase. Cells within the layer thereupon become increasingly free to attain their preferred shapes, with both $\overline{AR}$ and the variability in *AR* increasing as the cell layer becomes progressively more and more unjammed (Fig. S12). When propulsive forces become large enough they can unjam the jammed layer, and they do so with much the same implications for cell shape.[9,25,26,74,75] For a wide range of cases (Fig. S12), this computational approach provides independent confirmation of: 1) a linear relationship between SD(*AR*) and $\overline{AR}$, much as in Eq. 2 and Fig. 3g (inset), 2) a range of probability density functions all of which are concordant with the *k*-gamma distribution, much as in Eq. 1 and Fig. 3g, and, as determined from MLE analysis, 3) collapse of those predicted probability density functions to a universal distribution characterized by a single numerical value of *k* (Fig. 3h). And although this computational approach is in many regards overly simplistic, it makes a quantitative prediction concerning the numerical value of *k* (2.53), a value that slightly overestimates observations in HBECs and MDCKs but is in accord with observations in *Drosophila* embryos.

Detailed Description of Theoretical Model:

Here we simulate tissue configurations using a recent version of the Self-Propelled Voronoi (SPV) model.[26] In the SPV model, the basic degrees of freedom are the set of cell center positions $\{\vec{r}_i\}$ and cell shapes are given by Voronoi tessellation of the point pattern $\{\vec{r}_i\}$. The complex biomechanics that govern intracell and intercell interactions can be coarse-grained[25,26] and expressed in terms of a mechanical energy functional for individual cell shapes. For a multicell tissue given by a collection of cell areas (A_i) and cell perimeters (P_i), the energy functional is given by

$$E = \sum K_A(A_i - A_0)^2 + K_P(P_i - P_0)^2$$

The quadratic area term in the above equation accounts for a cell's resistance to volume changes via an area elastic modulus of K_A and a homeostatically preferred cell area A_0.[25,26]

Changes to a cell's perimeter are directly related to the deformation of the acto-myosin cortex concentrated near the cell membrane. The terms $K_P {P_i}^2$ corresponds to the elastic energy associated with deforming the cortex. The linear term in cell perimeter, $-K_0 P_0\ P_i$, represents the effective line tension in the cortex and gives rise to a `preferred perimeter' P_0. The value of P_0 can be decreased by up-regulating the contractile tension in the cortex[25,26] and it can be increased by up-regulating cell-cell adhesion.

In this work, we focus on cell shapes in the SPV in the limit of vanishing cell motility forces. We simulate a tissue containing N=400 cells under periodic boundary conditions with box size L = 20. The area modulus K_A is set to 0 to simulate the large variability of cell areas observed in HBEC cells (Fig. 1). We also set $K_P = 1$. With these choices for the model parameters, the characteristic lengthscale in the

system is related to the average area occupied by a cells $\langle A \rangle = L^2 / N = 1$, which is used as the unit length for all simulations. The reduced preferred cell perimeter $p_0 = P_0/\langle A \rangle$ is varied between 3.6 and 4.3. Initially, cell centers are randomly placed according to a Poisson point process and then evolved to energy minimum using the Broyden–Fletcher–Goldfarb–Shanno method.[77]
It has been shown that by changing the value of the preferred cell perimeter p_0, tissues undergo a solid-fluid transition.[25] This transition occurs at a critical value of $p_0 = 3.81$, and persist with finite cell motility forces.[26] When $p_0 < 3.81$ the tissue behaves as a rigid solid with a finite shear modulus and there are finite energetic barriers for a cell to move or rearrange. For $p_0 > 3.81$ the tissue becomes a fluid, with a vanishing shear modulus (Fig. S12).
The PDFs of the rescaled AR from the SPV model (Fig. 3g) can be well described by the k-gamma distribution (Eq.1). The value of k-parameter is obtained through least-squares fitting and displayed in Fig. S12b. There is a weak but systematic dependence of the value of k on the parameter P_0. When jammed ($P_0 < 3.81$), k stays a constant at value of 2.4. However in the unjammed state, k decreases as P_0 is increased and appear to approach a lower plateau value of 1.8 in the limit of large P_0. The small value of k may be related to the fact that spatial correlations cell AR decay quickly as a function of distance between two cells. To check to see if this is indeed the case, we calculate two-point spatial correlations for the SPV model (not shown). We observe that regardless of distance to the jamming transition, cell aspect ratios are always short-ranged and never persist beyond 2-cell diameters.

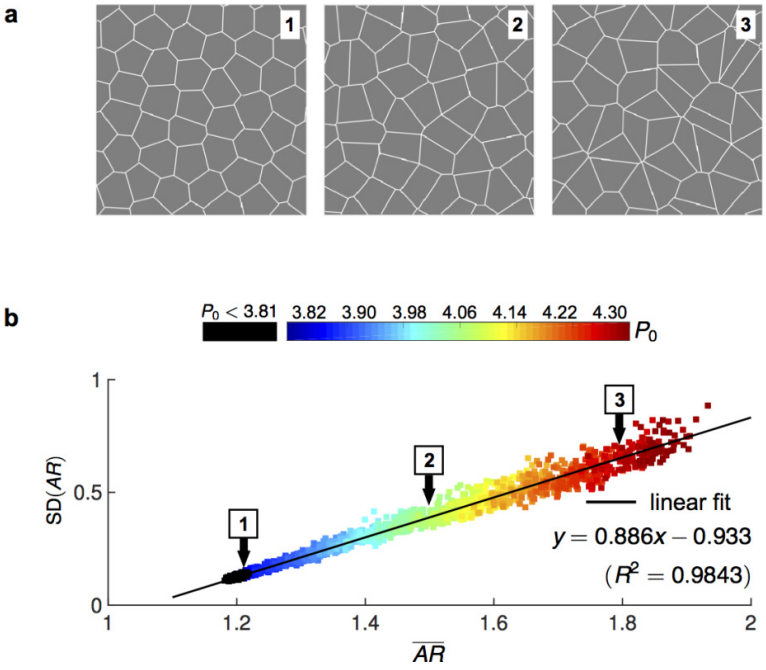

Figure S12| The self-propelled Voronoi (SPV) model [26] predicts a linear relationship between $\overline{AR}$ and $\mathrm{SD}(AR)$. While there are a variety of adjustable parameters that can be assigned in this model, this prediction is independent of those assigned values, and therefore requires no assignment of adjustable parameters and does not depend upon curve fitting. The position of the cellular system along this relationship is predicted to be set by proximity to the jamming transition.
a, Typical simulation snapshots are shown, corresponding to $P_0 = 3.81$ (at the onset of jamming), $P_0 = 4.05$ and $P_0 = 4.25$ (both fluid-like). **b**, Mean and SD of cell ARs from the SPV model are plotted for a large range of P_0 values. For $P_0 < 3.81$, the tissue is jammed where the mean aspect ratio (black line) remains nearly constant at 1.2. For $P_0 > 3.81$, the tissue unjamms and becomes more fluid-like. SD(*AR*) grows linearly with $\overline{AR}$ and can be fitted to the linear relationship shown in the figure (black line). Labels 1-3 correspond to the AR values of the snapshots shown in **a**. The shear modulus of the tissue decreases as P_0 is increased and vanishes for $P_0 > 3.81$, indicating an ujamming rigidity transition.[25,26]

7. *Supplementary Videos*

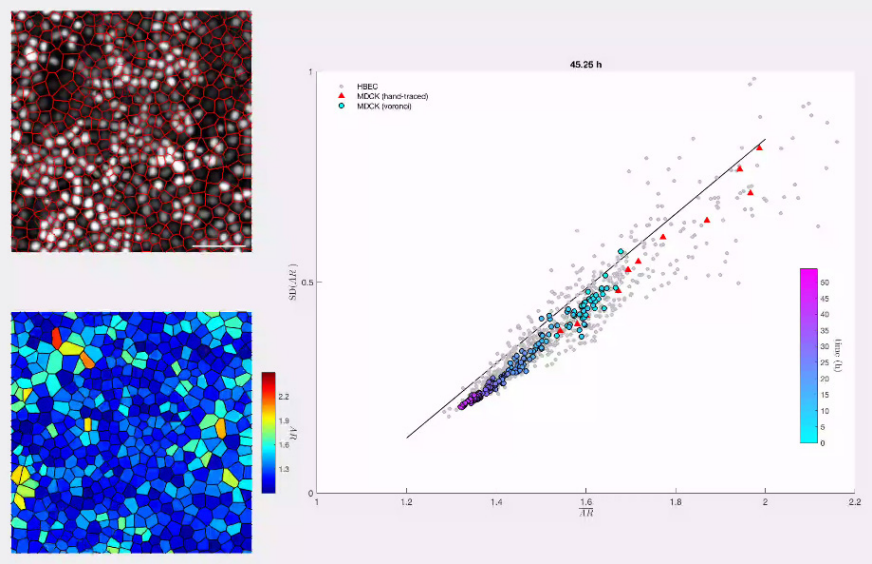

Video 1| Proliferating Madin Darby Canine Kidney (MDCK) cells follow the same relationship as HBEC cells (Figure 1) with shape and shape variability mutually constrained. $\overline{AR}$ decreased with time, but the relationship between $\overline{AR}$ and SD(*AR*) remained constrained. Top left panel: GFP nuclei with tessellated cells overlaid in red. Cells are only considered if resultant tiles have an area <1500 μm^2. Bottom left panel: corresponding color maps of *AR*, 10 to 64 hours after seeding are presented. Right panel: Each successive green datum represents $\overline{AR}$ vs SD(*AR*) with increasing time. Time 0 marks the beginning of the observation window in the fluorescent channel. Triangles: represents $\overline{AR}$ vs SD(*AR*) as acquired from manual tracing of cell boundaries from 12 fields of view with increasing time, in the corresponding phase channel. Gray: HBEC data. The black line is a theoretical prediction. Scale bar, 100 μm.

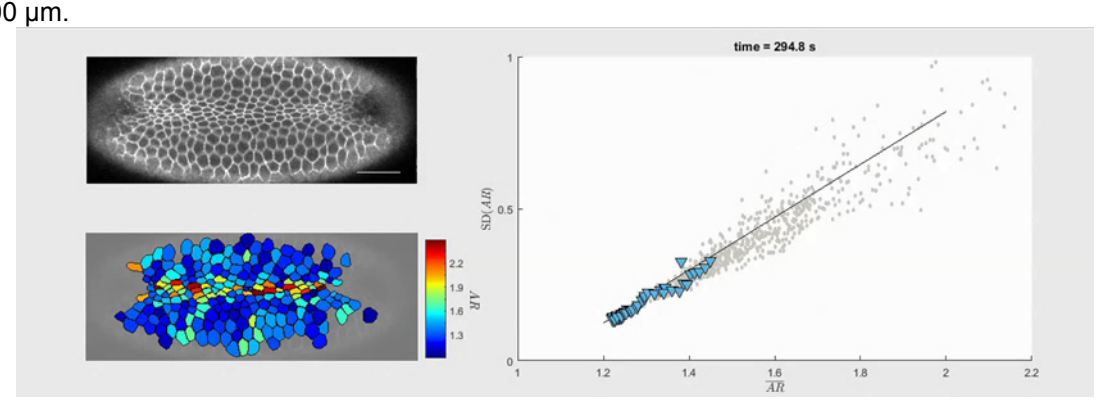

Video 2| During ventral furrow formation in this WT *Drosophila* embryo, cell aspect ratio follows the same relationship as HBEC cells with shape and shape variability mutually constrained. This video accompanies data presented in Figure 2 (a-c, left column). The relationship between $\overline{AR}$ and SD(*AR*) follows the same relationship as do HBECs, but in the opposite direction with time. Top left panel: z-projection of 3 consecutive slices imaging the ventral side of the embryo as cells constrict and attempt to form the ventral furrow (Fig. 2a,b left column). Data is presented until well before the furrow forms, when all cells are roughly in the same z-plane. Bottom left panel: corresponding color maps of *AR*. Right panel: Each successive blue datum represents $\overline{AR}$ vs SD(*AR*) with increasing time. Time as indicated, time 0 marks the beginning of the observation window. Gray: HBEC data. The black line is a theoretical prediction.

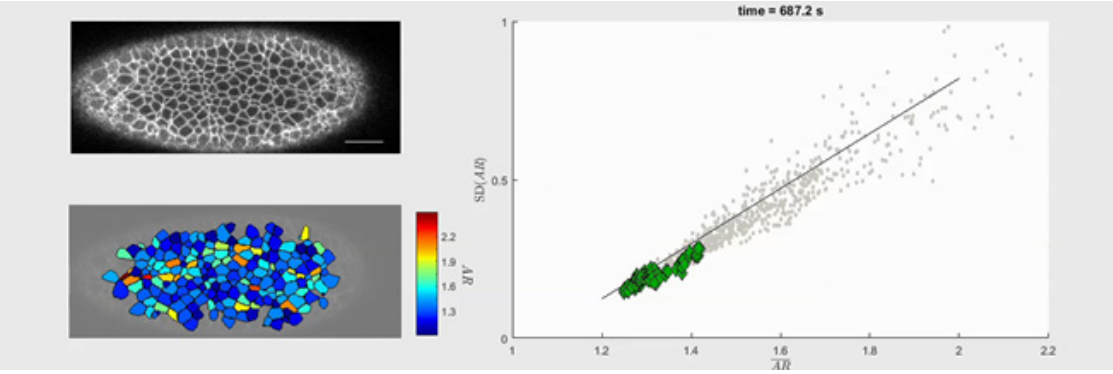

Video 3| While cells in this *cta* mutant *Drosophila* embryo attempt to form the ventral furrow, cell aspect ratio follows the same relationship as HBEC cells with shape and shape variability mutually constrained. This video accompanies data presented in Figure 2 (a-c, center column). The relationship between $\overline{AR}$ and SD(*AR*) follows the same relationship as do HBECs, but in the opposite direction with time. Additionally, these data follow the same relationship as Wild Type embryos, even though furrow formation is defective. Top left panel: z-projection of 3 consecutive slices imaging the ventral side of the embryo as cells constrict (Fig. 2a,b center column). Data is presented when all cells are roughly in the same z-plane. Bottom left panel: corresponding color maps of *AR*. Right panel: Each successive green datum represents $\overline{AR}$ vs SD(*AR*) with increasing time. Gray: HBEC data. Time as indicated, time 0 marks the beginning of the observation window. The black line is a theoretical prediction.

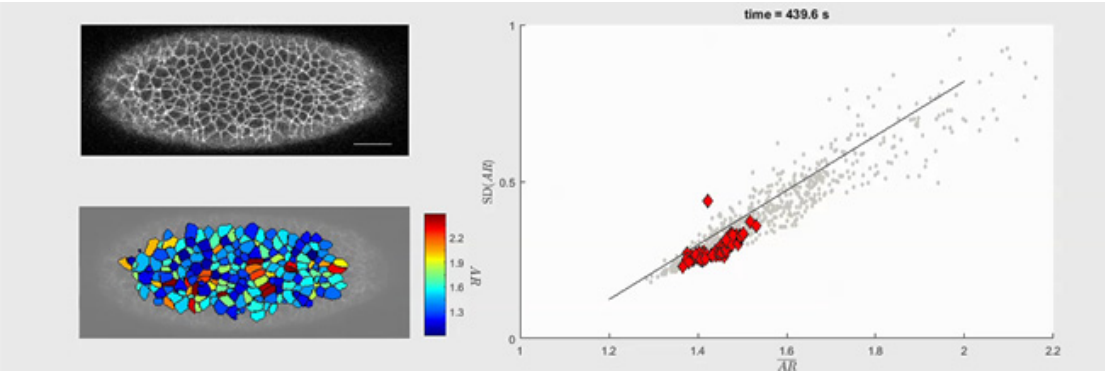

Video 4| While cells in this *twist* RNAi *Drosophila* embryo attempt to form the ventral furrow, cell aspect ratio follows the same relationship as HBEC cells, with shape and shape variability becoming mutually constrained. This video accompanies data presented in Figure 2 (a-c, right column). The relationship between $\overline{AR}$ and SD(*AR*) follows the same relationship as do HBECs, but in the opposite direction with time. Additionally, these data follow the same relationship as Wild Type embryos, even though furrow formation is hindered. Top left panel: z-projection of 3 consecutive slices imaging the ventral side of the embryo as cells constrict (Fig. 2a,b center column). Data is presented when all cells are roughly in the same z-plane. Bottom left panel: corresponding color maps of *AR*. Right panel: Each successive red datum represents $\overline{AR}$ vs SD(*AR*) with increasing time. Time as indicated, time 0 marks the beginning of the observation window. Gray: HBEC data. The black line is a theoretical prediction.

Supplementary References

49 Wong, I. Y. et al. Collective and individual migration following the epithelial–mesenchymal transition. Nat Mater advance online publication, doi:10.1038/nmat4062 (2014).

50 Reinhart-King, C. A. How matrix properties control the self-assembly and maintenance of tissues. Ann Biomed Eng 39, 1849-1856, doi:10.1007/s10439-011-0310-9 (2011).

51 Steward, R., Jr., Tambe, D., Hardin, C. C., Krishnan, R. & Fredberg, J. J. Fluid shear, intercellular stress, and endothelial cell alignment. Am J Physiol Cell Physiol 308, C657-664, doi:10.1152/ajpcell.00363.2014 (2015).

52 Cetera, M. & Horne-Badovinac, S. Round and round gets you somewhere: collective cell migration and planar polarity in elongating Drosophila egg chambers. Curr Opin Genet Dev 32, 10-15, doi:10.1016/j.gde.2015.01.003 (2015).

53 Campbell, K. & Casanova, J. A common framework for EMT and collective cell migration. Development 143, 4291-4300, doi:10.1242/dev.139071 (2016).

54 Thiery, J. P., Acloque, H., Huang, R. Y. & Nieto, M. A. Epithelial-mesenchymal transitions in development and disease. Cell 139, 871-890, doi:10.1016/j.cell.2009.11.007 (2009).

55 Jolly, M. K. et al. Implications of the Hybrid Epithelial/Mesenchymal Phenotype in Metastasis. Frontiers in Oncology 5, doi:10.3389/fonc.2015.00155 (2015).

56 Lambert, A. W., Pattabiraman, D. R. & Weinberg, R. A. Emerging Biological Principles of Metastasis. Cell 168, 670-691, doi:10.1016/j.cell.2016.11.037 (2017).

57 Rossen, N. S., Tarp, J. M., Mathiesen, J., Jensen, M. H. & Oddershede, L. B. Long-range ordered vorticity patterns in living tissue induced by cell division. Nature communications 5, 5720, doi:10.1038/ncomms6720 (2014).

58 Gudipaty, S. A. et al. Mechanical stretch triggers rapid epithelial cell division through Piezo1. Nature 543, 118-121, doi:10.1038/nature21407 (2017).

59 Eisenhoffer, G. T. et al. Crowding induces live cell extrusion to maintain homeostatic cell numbers in epithelia. Nature 484, 546-549, doi:10.1038/nature10999 (2012).

60 Gamboa Castro, M., Leggett, S. E. & Wong, I. Y. Clustering and jamming in epithelial-mesenchymal co-cultures. Soft matter 12, 8327-8337, doi:10.1039/c6sm01287f (2016).

61 Berthier, L. et al. Direct experimental evidence of a growing length scale accompanying the glass transition. Science 310, 1797-1800 (2005).

62 Tarjus, G., Schaaf, P. & Talbot, J. Random sequential addition: A distribution function approach. Journal of Statistical Physics 63, 167-202, doi:10.1007/BF01026598 (1991).

63 Xu, W.-S., Sun, Z.-Y. & An, L.-J. Relaxation dynamics in a binary hard-ellipse liquid. Soft matter 11, 627-634, doi:10.1039/C4SM02290D (2015).

64 Moučka, F. & Nezbeda, I. Detection and Characterization of Structural Changes in the Hard-Disk Fluid under Freezing and Melting Conditions. Physical Review Letters 94, 040601 (2005).

65 Atkinson, S., Stillinger, F. H. & Torquato, S. Existence of isostatic, maximally random jammed monodisperse hard-disk packings. Proc Natl Acad Sci U S A 111, 18436-18441, doi:10.1073/pnas.1408371112 (2014).

66 Gherardi, M. & Lagomarsino, M. C. Characterizing the size and shape of sea ice floes. Scientific Reports 5, 10226, doi:10.1038/srep10226 (2015).

67 Rackley, C. R. & Stripp, B. R. Building and maintaining the epithelium of the lung. J Clin Invest 122, 2724-2730, doi:10.1172/JCI60519 (2012).

68 Mertens, T. C. J., Karmouty-Quintana, H., Taube, C. & Hiemstra, P. S. Use of airway epithelial cell culture to unravel the pathogenesis and study treatment in obstructive airway diseases. Pulmonary Pharmacology & Therapeutics 45, 101-113, doi:10.1016/j.pupt.2017.05.008 (2017).

69 Xu, W. L. et al. A novel method for pulmonary research: Assessment of bioenergetic function at the air-liquid interface. Redox Biology 2, 513-519, doi:10.1016/j.redox.2014.01.004 (2014).

70 Frangi, A. F., Niessen, W. J., Vincken, K. L. & Viergever, M. Multiscale vessel enhancement filtering. Vol. 1496 130-137 (1998).

71 Teixidó, N. et al. Hierarchical segmentation-based software for cover classification analyses of seabed images (Seascape). MARINE ECOLOGY PROGRESS SERIES 431, 45–53 (2011).
72 Kaliman, S., Jayachandran, C., Rehfeldt, F. & Smith, A.-S. Limits of Applicability of the Voronoi Tessellation Determined by Centers of Cell Nuclei to Epithelium Morphology. Frontiers in Physiology 7, doi:10.3389/fphys.2016.00551 (2016).
73 Grainge, C. L. et al. Effect of bronchoconstriction on airway remodeling in asthma. N Engl J Med 364, 2006-2015, doi:10.1056/NEJMoa1014350 (2011).
74 Brodland, G. W. The Differential Interfacial Tension Hypothesis (DITH): a comprehensive theory for the self-rearrangement of embryonic cells and tissues. J Biomech Eng 124, 188-197 (2002).
75 Fletcher, A. G., Osterfield, M., Baker, R. E. & Shvartsman, S. Y. Vertex models of epithelial morphogenesis. Biophys J 106, 2291-2304, doi:10.1016/j.bpj.2013.11.4498 (2014).
76 Lecuit, T. & Lenne, P. F. Cell surface mechanics and the control of cell shape, tissue patterns and morphogenesis. Nature Reviews Molecular Cell Biology 8, 633-644, doi:10.1038/nrm2222 (2007).
77 Byrd, R. H., Lu, P. H., Nocedal, J. & Zhu, C. Y. A limited memeorey algortihm for bound constrained optimization. Siam Journal on Scientific Computing 16, 1190-1208, doi:10.1137/0916069 (1995).